

Measurement of the high-energy all-flavor neutrino-nucleon cross section with IceCube

R. Abbasi,¹⁷ M. Ackermann,⁵⁷ J. Adams,¹⁸ J. A. Aguilar,¹² M. Ahlers,²² M. Ahrens,⁴⁸ C. Alispach,²⁸ A. A. Alves, Jr.,³¹ N. M. Amin,⁴¹ K. Andeen,³⁹ T. Anderson,⁵⁴ I. Ansseau,¹² G. Anton,²⁶ C. Argüelles,¹⁴ S. Axani,¹⁵ X. Bai,⁴⁵ A. Balagopal V.,³⁷ A. Barbano,²⁸ S. W. Barwick,³⁰ B. Bastian,⁵⁷ V. Basu,³⁷ V. Baum,³⁸ S. Baur,¹² R. Bay,⁸ J. J. Beatty,^{20,21} K.-H. Becker,⁵⁶ J. Becker Tjus,¹¹ C. Bellenghi,²⁷ S. Ben Zvi,⁴⁷ D. Berley,¹⁹ E. Bernardini,^{57,*} D. Z. Besson,^{32,†} G. Binder,^{8,9} D. Bindig,⁵⁶ E. Blaufuss,¹⁹ S. Blot,⁵⁷ S. Böser,³⁸ O. Botner,⁵⁵ J. Böttcher,¹ E. Bourbeau,²² J. Bourbeau,³⁷ F. Bradascio,⁵⁷ J. Braun,³⁷ S. Bron,²⁸ J. Brostean-Kaiser,⁵⁷ A. Burgman,⁵⁵ R. S. Busse,⁴⁰ M. A. Campana,⁴⁴ C. Chen,⁶ D. Chirkin,³⁷ S. Choi,⁵⁰ B. A. Clark,²⁴ K. Clark,³³ L. Classen,⁴⁰ A. Coleman,⁴¹ G. H. Collin,¹⁵ J. M. Conrad,¹⁵ P. Coppin,¹³ P. Correa,¹³ D. F. Cowen,^{53,54} R. Cross,⁴⁷ P. Dave,⁶ C. De Clercq,¹³ J. J. DeLaunay,⁵⁴ H. Dembinski,⁴¹ K. Deoskar,⁴⁸ S. De Ridder,²⁹ A. Desai,³⁷ P. Desiati,³⁷ K. D. de Vries,¹³ G. de Wasseige,¹³ M. de With,¹⁰ T. DeYoung,²⁴ S. Dharani,¹ A. Diaz,¹⁵ J. C. Díaz-Vélez,³⁷ H. Dujmovic,³¹ M. Dunkman,⁵⁴ M. A. DuVernois,³⁷ E. Dvorak,⁴⁵ T. Ehrhardt,³⁸ P. Eller,²⁷ R. Engel,³¹ J. Evans,¹⁹ P. A. Evenson,⁴¹ S. Fahey,³⁷ A. R. Fazely,⁷ S. Fiedlschuster,²⁶ A. T. Fienberg,⁵⁴ K. Filimonov,⁸ C. Finley,⁴⁸ L. Fischer,⁵⁷ D. Fox,⁵³ A. Franckowiak,^{11,57} E. Friedman,¹⁹ A. Fritz,³⁸ P. Fürst,¹ T. K. Gaisser,⁴¹ J. Gallagher,³⁶ E. Ganster,¹ S. Garrappa,⁵⁷ L. Gerhardt,⁹ A. Ghadimi,⁵² T. Glauch,²⁷ T. Glüsenkamp,²⁶ A. Goldschmidt,⁹ J. G. Gonzalez,⁴¹ S. Goswami,⁵² D. Grant,²⁴ T. Grégoire,⁵⁴ Z. Griffith,³⁷ S. Griswold,⁴⁷ M. Gündüz,¹¹ C. Haack,²⁷ A. Hallgren,⁵⁵ R. Halliday,²⁴ L. Halve,¹ F. Halzen,³⁷ M. Ha Minh,²⁷ K. Hanson,³⁷ J. Hardin,³⁷ A. Haungs,³¹ S. Hauser,¹ D. Hebecker,¹⁰ K. Helbing,⁵⁶ F. Henningsen,²⁷ S. Hickford,⁵⁶ J. Hignight,²⁵ C. Hill,¹⁶ G. C. Hill,² K. D. Hoffman,¹⁹ R. Hoffmann,⁵⁶ T. Hoinka,²³ B. Hokanson-Fasig,³⁷ K. Hoshina,^{37,‡} F. Huang,⁵⁴ M. Huber,²⁷ T. Huber,³¹ K. Hultqvist,⁴⁸ M. Hünnefeld,²³ R. Hussain,³⁷ S. In,⁵⁰ N. Iovine,¹² A. Ishihara,¹⁶ M. Jansson,⁴⁸ G. S. Japaridze,⁵ M. Jeong,⁵⁰ B. J. P. Jones,⁴ R. Joppe,¹ D. Kang,³¹ W. Kang,⁵⁰ X. Kang,⁴⁴ A. Kappes,⁴⁰ D. Kappesser,³⁸ T. Karg,⁵⁷ M. Karl,²⁷ A. Karle,³⁷ U. Katz,²⁶ M. Kauer,³⁷ M. Kellermann,¹ J. L. Kelley,³⁷ A. Kheirandish,⁵⁴ J. Kim,⁵⁰ K. Kin,¹⁶ T. Kintscher,⁵⁷ J. Kiryluk,⁴⁹ S. R. Klein,^{8,9} R. Koirala,⁴¹ H. Kolanoski,¹⁰ L. Köpke,³⁸ C. Kopper,²⁴ S. Kopper,⁵² D. J. Koskinen,²² P. Koundal,³¹ M. Kovacevich,⁴⁴ M. Kowalski,^{10,57} K. Krings,²⁷ G. Krückl,³⁸ N. Kulacz,²⁵ N. Kurahashi,⁴⁴ A. Kyriacou,² C. Lagunas Gualda,⁵⁷ J. L. Lanfranchi,⁵⁴ M. J. Larson,¹⁹ F. Lauber,⁵⁶ J. P. Lazar,^{14,37} K. Leonard,³⁷ A. Leszczyńska,³¹ Y. Li,⁵⁴ Q. R. Liu,³⁷ E. Lohfink,³⁸ C. J. Lozano Mariscal,⁴⁰ L. Lu,¹⁶ F. Lucarelli,²⁸ A. Ludwig,^{24,34} W. Luszczak,³⁷ Y. Lyu,^{8,9} W. Y. Ma,⁵⁷ J. Madsen,⁴⁶ K. B. M. Mahn,²⁴ Y. Makino,³⁷ P. Mallik,¹ S. Mancina,³⁷ I. C. Mariş,¹² R. Maruyama,⁴² K. Mase,¹⁶ F. McNally,³⁵ K. Meagher,³⁷ A. Medina,²¹ M. Meier,¹⁶ S. Meighen-Berger,²⁷ J. Merz,¹ J. Micallef,²⁴ D. Mockler,¹² G. Momenté,³⁸ T. Montaruli,²⁸ R. W. Moore,²⁵ R. Morse,³⁷ M. Moulai,¹⁵ R. Naab,⁵⁷ R. Nagai,¹⁶ U. Naumann,⁵⁶ J. Necker,⁵⁷ G. Neer,²⁴ L. V. Nguyen,²⁴ H. Niederhausen,²⁷ M. U. Nisa,²⁴ S. C. Nowicki,²⁴ D. R. Nygren,⁹ A. Obertacke Pollmann,⁵⁶ M. Oehler,³¹ A. Olivas,¹⁹ E. O'Sullivan,⁵⁵ H. Pandya,⁴¹ D. V. Pankova,⁵⁴ N. Park,³⁷ G. K. Parker,⁴ E. N. Paudel,⁴¹ P. Peiffer,³⁸ C. Pérez de los Heros,⁵⁵ S. Philippen,¹ D. Pieloth,²³ S. Pieper,⁵⁶ A. Pizzuto,³⁷ M. Plum,³⁹ Y. Popovych,¹ A. Porcelli,²⁹ M. Prado Rodriguez,³⁷ P. B. Price,⁸ G. T. Przybylski,⁹ C. Raab,¹² A. Raissi,¹⁸ M. Rameez,²² K. Rawlins,³ I. C. Rea,²⁷ A. Rehman,⁴¹ R. Reimann,¹ M. Renschler,³¹ G. Renzi,¹² E. Resconi,²⁷ S. Reusch,⁵⁷ W. Rhode,²³ M. Richman,⁴⁴ B. Riedel,³⁷ S. Robertson,^{8,9} G. Roellinghoff,⁵⁰ M. Rongen,¹ C. Rott,⁵⁰ T. Ruhe,²³ D. Ryckbosch,²⁹ D. Rysewyk Cantu,²⁴ I. Safa,^{14,37} S. E. Sanchez Herrera,²⁴ A. Sandrock,²³ J. Sandroos,³⁸ M. Santander,⁵² S. Sarkar,⁴³ S. Sarkar,²⁵ K. Satalecka,⁵⁷ M. Scharf,¹ M. Schaufel,¹ H. Schieler,³¹ P. Schlunder,²³ T. Schmidt,¹⁹ A. Schneider,³⁷ J. Schneider,²⁶ F. G. Schröder,^{31,41} L. Schumacher,¹ S. Sclafani,⁴⁴ D. Seckel,⁴¹ S. Seunarine,⁴⁶ S. Shefali,¹ M. Silva,³⁷ B. Smithers,⁴ R. Snihur,³⁷ J. Soedingrekso,²³ D. Soldin,⁴¹ G. M. Spiczak,⁴⁶ C. Spiering,^{57,†} J. Stachurska,⁵⁷ M. Stamatikos,²¹ T. Stanev,⁴¹ R. Stein,⁵⁷ J. Stettner,¹ A. Steuer,³⁸ T. Stezelberger,⁹ R. G. Stokstad,⁹ N. L. Strotjohann,⁵⁷ T. Stuttard,²² G. W. Sullivan,¹⁹ I. Taboada,⁶ F. Tenholt,¹¹ S. Ter-Antonyan,⁷ S. Tilav,⁴¹ F. Tischbein,¹ K. Tollefson,²⁴ L. Tomankova,¹¹ C. Tönnis,⁵¹ S. Toscano,¹² D. Tosi,³⁷ A. Tretin,⁵⁷ M. Tselengidou,²⁶ C. F. Tung,⁶ A. Turcati,²⁷ R. Turcotte,³¹ C. F. Turley,⁵⁴ J. P. Twagirayezu,²⁴ B. Ty,³⁷ E. Unger,⁵⁵ M. A. Unland Elorrieta,⁴⁰ M. Usner,⁵⁷ J. Vandenbroucke,³⁷ D. van Eijk,³⁷ N. van Eijndhoven,¹³ D. Vannerom,¹⁵ J. van Santen,⁵⁷ S. Verpoest,²⁹ M. Vraeghe,²⁹ C. Walck,⁴⁸ A. Wallace,² N. Wandkowsky,³⁷ T. B. Watson,⁴ C. Weaver,²⁵ A. Weindl,³¹ M. J. Weiss,⁵⁴ J. Weldert,³⁸ C. Wendt,³⁷ J. Werthebach,²³ M. Weyrauch,³¹ B. J. Whelan,² N. Whitehorn,^{24,34} K. Wiebe,³⁸ C. H. Wiebusch,¹ D. R. Williams,⁵² M. Wolf,²⁷ T. R. Wood,²⁵ K. Woschnagg,⁸ G. Wrede,²⁶ J. Wulff,¹¹ X. W. Xu,⁷ Y. Xu,⁴⁹ J. P. Yanez,²⁵ S. Yoshida,¹⁶ T. Yuan,³⁷ and Z. Zhang⁴⁹

(IceCube Collaboration)

¹*III. Physikalisches Institut, RWTH Aachen University, D-52056 Aachen, Germany*²*Department of Physics, University of Adelaide, Adelaide 5005, Australia*

- ³*Department of Physics and Astronomy, University of Alaska Anchorage,
3211 Providence Drive, Anchorage, Alaska 99508, USA*
- ⁴*Department of Physics, University of Texas at Arlington,
502 Yates Street, Science Hall Room 108, Box 19059, Arlington, Texas 76019, USA*
- ⁵*CTSPS, Clark-Atlanta University, Atlanta, Georgia 30314, USA*
- ⁶*School of Physics and Center for Relativistic Astrophysics, Georgia Institute of Technology,
Atlanta, Georgia 30332, USA*
- ⁷*Department of Physics, Southern University, Baton Rouge, Louisiana 70813, USA*
- ⁸*Department of Physics, University of California, Berkeley, California 94720, USA*
- ⁹*Lawrence Berkeley National Laboratory, Berkeley, California 94720, USA*
- ¹⁰*Institut für Physik, Humboldt-Universität zu Berlin, D-12489 Berlin, Germany*
- ¹¹*Fakultät für Physik & Astronomie, Ruhr-Universität Bochum, D-44780 Bochum, Germany*
- ¹²*Université Libre de Bruxelles, Science Faculty CP230, B-1050 Brussels, Belgium*
- ¹³*Vrije Universiteit Brussel (VUB), Dienst ELEM, B-1050 Brussels, Belgium*
- ¹⁴*Department of Physics and Laboratory for Particle Physics and Cosmology, Harvard University,
Cambridge, Massachusetts 02138, USA*
- ¹⁵*Department of Physics, Massachusetts Institute of Technology, Cambridge, Massachusetts 02139, USA*
- ¹⁶*Department of Physics and Institute for Global Prominent Research, Chiba University,
Chiba 263-8522, Japan*
- ¹⁷*Department of Physics, Loyola University Chicago, Chicago, Illinois 60660, USA*
- ¹⁸*Department of Physics and Astronomy, University of Canterbury,
Private Bag 4800, Christchurch, New Zealand*
- ¹⁹*Department of Physics, University of Maryland, College Park, Maryland 20742, USA*
- ²⁰*Department of Astronomy, Ohio State University, Columbus, Ohio 43210, USA*
- ²¹*Department of Physics and Center for Cosmology and Astro-Particle Physics, Ohio State University,
Columbus, Ohio 43210, USA*
- ²²*Niels Bohr Institute, University of Copenhagen, DK-2100 Copenhagen, Denmark*
- ²³*Department of Physics, TU Dortmund University, D-44221 Dortmund, Germany*
- ²⁴*Department of Physics and Astronomy, Michigan State University, East Lansing, Michigan 48824, USA*
- ²⁵*Department of Physics, University of Alberta, Edmonton, Alberta T6G 2E1, Canada*
- ²⁶*Erlangen Centre for Astroparticle Physics, Friedrich-Alexander-Universität Erlangen-Nürnberg,
D-91058 Erlangen, Germany*
- ²⁷*Physik-department, Technische Universität München, D-85748 Garching, Germany*
- ²⁸*Département de physique nucléaire et corpusculaire, Université de Genève,
CH-1211 Genève, Switzerland*
- ²⁹*Department of Physics and Astronomy, University of Gent, B-9000 Gent, Belgium*
- ³⁰*Department of Physics and Astronomy, University of California, Irvine, California 92697, USA*
- ³¹*Karlsruhe Institute of Technology, Institute for Astroparticle Physics, D-76021 Karlsruhe, Germany*
- ³²*Department of Physics and Astronomy, University of Kansas, Lawrence, Kansas 66045, USA*
- ³³*SNOLAB, 1039 Regional Road 24, Creighton Mine 9, Lively, Ontario P3Y 1N2, Canada*
- ³⁴*Department of Physics and Astronomy, UCLA, Los Angeles, California 90095, USA*
- ³⁵*Department of Physics, Mercer University, Macon, Georgia 31207-0001, USA*
- ³⁶*Department of Astronomy, University of Wisconsin–Madison, Madison, Wisconsin 53706, USA*
- ³⁷*Department of Physics and Wisconsin IceCube Particle Astrophysics Center,
University of Wisconsin–Madison, Madison, Wisconsin 53706, USA*
- ³⁸*Institute of Physics, University of Mainz, Staudinger Weg 7, D-55099 Mainz, Germany*
- ³⁹*Department of Physics, Marquette University, Milwaukee, Wisconsin 53201, USA*
- ⁴⁰*Institut für Kernphysik, Westfälische Wilhelms-Universität Münster, D-48149 Münster, Germany*
- ⁴¹*Bartol Research Institute and Dept. of Physics and Astronomy, University of Delaware,
Newark, Delaware 19716, USA*
- ⁴²*Department of Physics, Yale University, New Haven, Connecticut 06520, USA*
- ⁴³*Department of Physics, University of Oxford, Parks Road, Oxford OX1 3PU, United Kingdom*
- ⁴⁴*Department of Physics, Drexel University,
3141 Chestnut Street, Philadelphia, Pennsylvania 19104, USA*
- ⁴⁵*Physics Department, South Dakota School of Mines and Technology,
Rapid City, South Dakota 57701, USA*
- ⁴⁶*Department of Physics, University of Wisconsin, River Falls, Wisconsin 54022, USA*
- ⁴⁷*Department of Physics and Astronomy, University of Rochester, Rochester, New York 14627, USA*
- ⁴⁸*Oskar Klein Centre and Department of Physics, Stockholm University, SE-10691 Stockholm, Sweden*

⁴⁹*Department of Physics and Astronomy, Stony Brook University,
Stony Brook, New York 11794-3800, USA*

⁵⁰*Department of Physics, Sungkyunkwan University, Suwon 16419, Korea*

⁵¹*Institute of Basic Science, Sungkyunkwan University, Suwon 16419, Korea*

⁵²*Department of Physics and Astronomy, University of Alabama, Tuscaloosa, Alabama 35487, USA*

⁵³*Department of Astronomy and Astrophysics, Pennsylvania State University,
University Park, Pennsylvania 16802, USA*

⁵⁴*Department of Physics, Pennsylvania State University, University Park, Pennsylvania 16802, USA*

⁵⁵*Department of Physics and Astronomy, Uppsala University, Box 516, S-75120 Uppsala, Sweden*

⁵⁶*Department of Physics, University of Wuppertal, D-42119 Wuppertal, Germany*

⁵⁷*DESY, D-15738 Zeuthen, Germany*



(Received 16 November 2020; accepted 9 February 2021; published 8 July 2021)

The flux of high-energy neutrinos passing through the Earth is attenuated due to their interactions with matter. The interaction rate is determined by the neutrino interaction cross section and affects the flux arriving at the IceCube Neutrino Observatory, a cubic-kilometer neutrino detector embedded in the Antarctic ice sheet. We present a measurement of the neutrino cross section between 60 TeV and 10 PeV using the high-energy starting event (HESE) sample from IceCube with 7.5 years of data. The result is binned in neutrino energy and obtained using both Bayesian and frequentist statistics. We find it compatible with predictions from the Standard Model. While the cross section is expected to be flavor independent above 1 TeV, additional constraints on the measurement are included through updated experimental particle identification (PID) classifiers, proxies for the three neutrino flavors. This is the first such measurement to use a ternary PID observable and the first to account for neutrinos from tau decay.

DOI: [10.1103/PhysRevD.104.022001](https://doi.org/10.1103/PhysRevD.104.022001)

I. INTRODUCTION

In the Standard Model (SM), neutrino interactions are mediated by W^\pm and Z^0 bosons for charged-current (CC) and neutral-current (NC) channels, respectively. At energies above a few GeV, the dominant process is deep inelastic scattering (DIS) off of individual partons within the nucleon. Calculations in the perturbative QCD (pQCD) formalism rely on parton distribution functions (PDFs) obtained mostly from DIS experiments [1–3]. Uncertainties on the PDFs lead to uncertainties on the cross section. An alternative approach [4] based on an empirical color dipole model of the nucleon along with the assumption that all cross sections increase at high energies as $\ln^2 s$ results in good agreement with the latest pQCD calculations. Proposed extensions of the SM based on large extra dimensions opening up above the Fermi scale predict a sharp rise in the neutrino-nucleon cross section above the

SM value. One such model [5], which was motivated by the claimed detection of cosmic rays above the Greisen–Zatsepin–Kuzmin (GZK) bound, assumes that neutrino-nucleon interaction is mediated by a massive spin-2 boson. This allows the neutrino-nucleon cross section to climb above 10^{-27} cm^2 at $E_\nu > 10^{19} \text{ eV}$. Another possibility if spacetime has greater than four dimensions allows for the production of microscopic black holes in high-energy particle interactions and also leads to an increased neutrino-nucleon cross section above approximately 1 PeV [6]. Such scenarios where the cross section increases steeply with energy could also be due to the existence of exotic particles such as leptoquarks [7] or sphalerons [8], both of which have been discussed in the context of neutrino telescopes and could be probed via measurements of the high-energy neutrino cross section.

At energies above 40 TeV, the Earth becomes opaque to neutrinos. For a power-law spectrum proportional to $E^{-\gamma}$ at Earth's surface, the ratio of the flux arriving at IceCube to that at Earth's surface, $\Phi(E_\nu)/\Phi_0(E_\nu)$, depends on the Earth column density, neutrino energy, E_ν , spectral index γ (through secondaries), and neutrino cross section. The Earth column density is defined as $t(\theta) = \int_0^{y_{\max}} \rho(y, \theta) dy$, where θ is the arrival direction of the neutrino, y_{\max} is its path length through the Earth, and $\rho(y, \theta)$ is the density at a point y along the path. Figure 1 shows the electron neutrino and antineutrino $\Phi(E_\nu)/\Phi_0(E_\nu)$ assuming a surface flux with $\gamma = 2$, arising from Fermi acceleration at shocks [9,10]. The spectral index affects the arrival flux through

*Also at Università di Padova, I-35131 Padova, Italy.

†Also at National Research Nuclear University, Moscow Engineering Physics Institute (MEPhI), Moscow 115409, Russia.

‡Also at Earthquake Research Institute, University of Tokyo, Bunkyo, Tokyo 113-0032, Japan.

Published by the American Physical Society under the terms of the [Creative Commons Attribution 4.0 International](https://creativecommons.org/licenses/by/4.0/) license. Further distribution of this work must maintain attribution to the author(s) and the published article's title, journal citation, and DOI. Funded by SCOAP³.

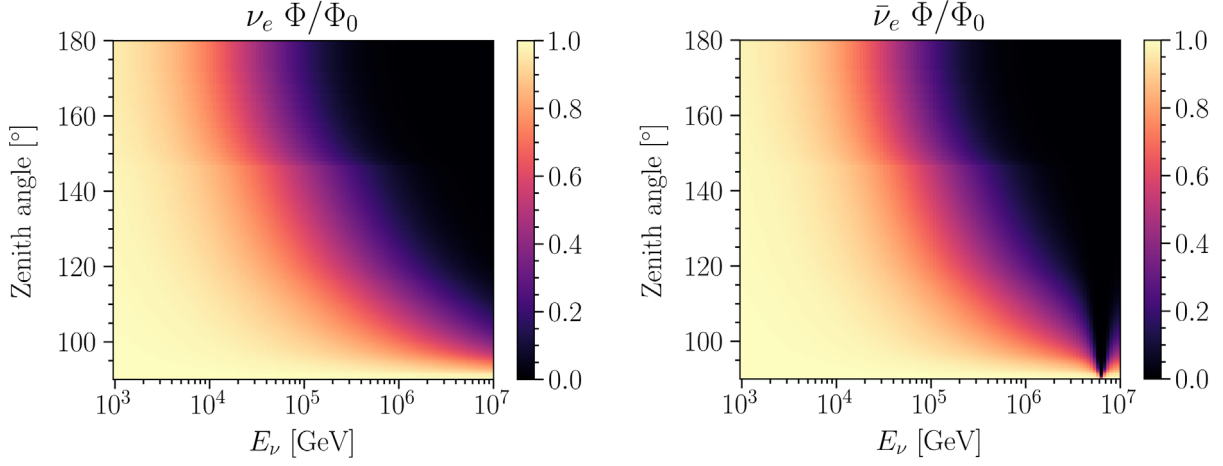


FIG. 1. Ratio of the arrival flux to surface flux for both electron neutrinos and antineutrinos as a function of E_ν and zenith angle in IceCube detector coordinates. The flux at the surface is assumed to have a spectral index of $\gamma = 2$. The core-mantle boundary is visible as a discontinuity near a zenith angle of 147° , and the enhanced suppression due to Glashow resonance is visible near 6.3 PeV in the electron antineutrino channel. Flux ratios for the other flavors are similar to that of electron neutrinos.

secondaries produced by tau decay in CC interactions or NC interactions. In ν_e and ν_μ CC interactions, the neutrino is effectively destroyed, whereas in ν_τ CC interactions, the outgoing tau-lepton may decay into lower-energy neutrinos [11]. In NC interactions, the incoming neutrino is not destroyed but cascades down in energy [12]. These flavor-dependent processes alter the neutrino flux as a function of the traversed path length [13], which allows for probing the neutrino cross section at high energies. The dip in the $\bar{\nu}_e$ flux ratio due to the Glashow resonance [14] is visible in the right panel of Fig. 1 near $E_\nu = 6.3$ PeV. The Glashow resonance occurs from the interaction of an electron antineutrino with a bound atomic electron and is independent of the CC and NC interactions of nucleons. A related, but subdominant, effect that has found renewed interest is the production of an on-shell W -boson off of the nucleus [15–18]. While this measurement is insensitive to the process, prospects for detection seem favorable with IceCube-Gen2 [19,20].

The IceCube Neutrino Observatory, an in-ice neutrino detector situated at the South Pole, is capable of detecting high-energy neutrinos originating from both Northern and Southern hemispheres [21–24]. IceCube comprises over 5000 digital optical modules (DOMs) encompassing approximately a cubic kilometer of ice [25–27]. The ice acts as a detection medium by which Cherenkov radiation from charged particles produced in neutrino interactions can be observed. The high-energy starting event (HESE) sample selects events that interact within a fiducial region of the detector across a 4π solid angle [24,28]. Here, we report a new cross section measurement using information from all three neutrino flavors with 7.5 years of data.

While SM calculations are generally consistent in the TeV–PeV energy range, few experimental measurements exist, and none have been performed with all three neutrino

flavors [29,30]. Recently, an IceCube measurement of the neutrino DIS cross section using up-going, muon neutrinos gave a result consistent with the Standard Model [29]. The measurement in Ref. [30] used showers in publicly available HESE data with six years of data taking. This result, using the latest HESE sample with 7.5 years of data, includes classifiers for all three neutrino flavors and accounts for neutrinos from NC interactions and tau regeneration. Out of a total of 60 events above 60 TeV, 33 are also used in Ref. [30]. However, updates described in Ref. [28] affect the measurement and are incorporated in this work. These include updated parametrizations of absorption and scattering of light in the ice [31,32], more accurate atmospheric neutrino passing fractions [33], a likelihood construction that properly accounts for the stochastic nature of IceCube simulations [34], and improved systematics treatment [35].

As the sample updates are detailed in Ref. [28], this paper focuses on the results of the neutrino-nucleon cross section measurement. A brief description of the event selection is given in Sec. II. Section III details the analysis procedure. Section IV presents our Bayesian and frequentist results and compares them to existing measurements. We conclude in Sec. V.

II. EVENT SELECTION

The measurements presented here rely on a sample of high-energy events that start within a fiducial region of the IceCube detector [24,28]. In this context, events are taken to be the interaction byproducts of neutrino interactions, or background muons from cosmic-ray interactions in the atmosphere. The 90 m of the top and outer side layers of the detector, 10 m of the bottom of the detector, and a 60 m horizontal region near the highest concentration of dust in the ice are used as an active veto. Only events with fewer

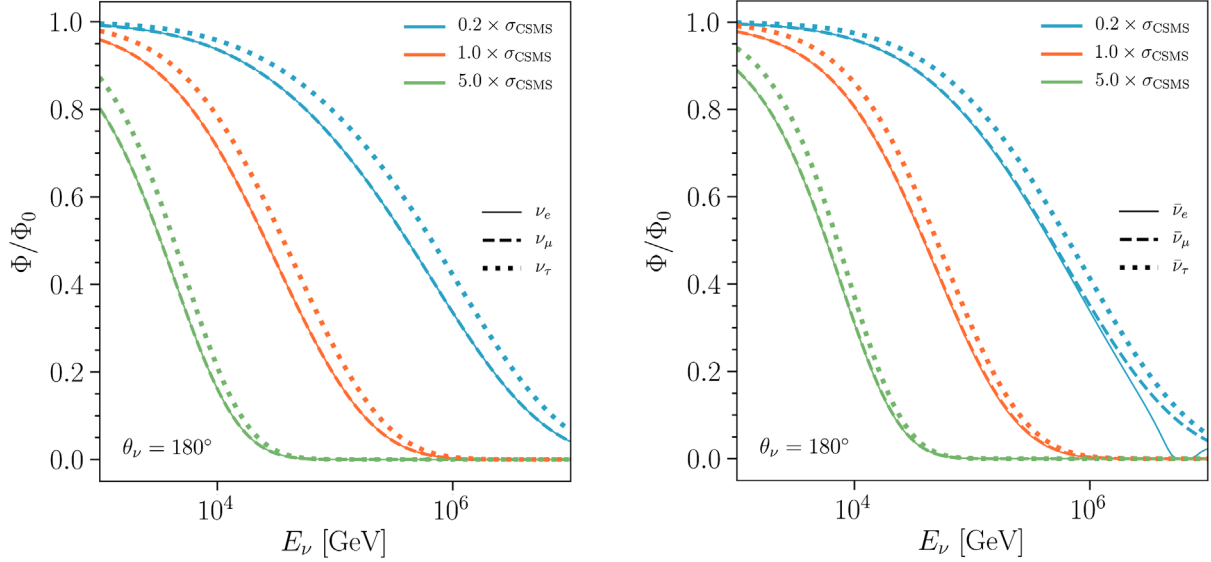


FIG. 2. Ratio of the arrival flux to surface flux for both neutrinos and antineutrinos as a function of E_ν for three realizations of the cross section. The flux at the surface is assumed to have a spectral index of $\gamma = 2$. The scaling is applied to the cross section given by Cooper-Sarkar *et al.* (CSMS) [2].

than 3 photoelectrons (PEs) and fewer than 3 hit DOMs in the veto region within a predefined time window are kept. In addition, the total charge must exceed 6000 PE [28]. This removes almost all of the background due to atmospheric muons from the Southern sky. Neutrinos arriving from above and below the detector are included in the sample, thus allowing for constraints across the full allowed region in zenith.

Events are grouped into three experimental particle identification (PID) classifiers: cascades, tracks, and double cascades. These PIDs are related to the true interaction channel of the neutrino. Electromagnetic and hadronic showers appear cascadelike, stochastic energy losses from high-energy muons appear tracklike, and the production and subsequent decay of a tau can appear as double cascades (in addition to the other two PIDs) [28,36]. Since a NC interaction produces a hadronic shower, it is not directly distinguishable from a CC interaction. In addition, misclassifications can occur, and as such, the mapping from true to reconstructed observables is imperfect. To model such effects, detailed Monte Carlo (MC) simulations are performed, taking into account systematic variations in the ice model. The MC is then processed in an identical manner as the data. It thus provides the connection from the physics parameters of interest to the observed data events.

III. ANALYSIS METHOD

The cross section is probed by measuring neutrino absorption in the Earth, which effects an angular and energy dependence in the neutrino flux arriving at IceCube. In essence, we perform fits to the measured

energy-zenith distribution for different hypotheses of the cross section, using a MC to model the expected signal under these hypotheses. A proper modeling accounts for neutrino interactions in the Earth as well as in the detector, with the event rate being proportional to the product of the cross section and the arrival flux. Knowledge of the number of events detected in data and the expected arrival flux can thus be used to measure the cross section. This is accomplished by binning the data and the expectation from MC (under a particular assumption of the cross section and flux) in observable space and then constructing a representative likelihood. The MC expectation varies as the cross section, as well as other systematic parameters, is modified. These modifications on theoretical parameters are captured via event-by-event reweighting of the MC [37]. For this analysis, the neutrino DIS cross section is parametrized as a function of four independent energy slices.

Figure 2 illustrates the effect of scaling the DIS cross section up or down on the survival probability as a function of energy for a neutrino traveling through the full diameter of the Earth. It is plotted for each flavor individually as a function of the neutrino energy, E_ν ; at a zenith angle of 180° ; and for a surface flux with spectral index of $\gamma = 2$. The dependence on the spectrum arises from secondary neutrinos, which cascade down in energy and are produced in NC interactions and tau decay [11]. As the cross section increases, $\Phi(E_\nu)/\Phi_0(E_\nu)$ decreases since the neutrinos are more likely to interact on their way through the Earth. The reason there is a slight flavor dependence is due to the fact that CC $\bar{\nu}_e$ and $\bar{\nu}_\mu$ interactions are destructive, while a CC $\bar{\nu}_\tau$ interaction produces a tau lepton, which, unlike

muons that lose most of their energy in the Earth before decaying due to their much longer lifetimes, can quickly decay to a lower-energy ν_τ . Neutral-current interactions have a similar effect, and these effects are taken into account [13,29]. Furthermore, the dip in the $\bar{\nu}_e$ flux ratio due to the Glashow resonance is again visible. This effect, taken over the full two-dimensional energy-zenith distribution, allows us to place constraints on the cross section itself.

In this paper, we report the neutrino DIS cross section as a function of energy under a single-power-law astrophysical flux assumption. Four scaling parameters, $\mathbf{x} = (x_0, x_1, x_2, x_3)$, are applied to the cross section given by CSMS [2] across four energy bins with edges fixed at 60 TeV, 100 TeV, 200 TeV, 500 TeV, and 10 PeV, where the indices correspond to the ordering of the energy bins from lowest to highest energies. Each parameter linearly scales the neutrino and antineutrino DIS cross section in each bin, while keeping the ratio of CC-to-NC contributions fixed. More specifically, for each \mathbf{x} , neutrino events in MC are reweighted by $x_i \Phi(E_\nu, \theta_\nu, \mathbf{x}) / \Phi(E_\nu, \theta_\nu, \mathbf{1})$, where Φ is the arrival flux as calculated by nuSQuIDS, E_ν is the true neutrino energy, θ_ν the true neutrino zenith angle, and x_i the cross section scaling factor at E_ν . The fixed CC-to-NC ratio implies that this analysis should not be interpreted as a direct test of the large extra dimensions model [5], which only applies to NC interactions. At energies above 1 TeV, the neutrino-nucleon cross sections for all three neutrino flavors converge. The cross section is therefore assumed to not depend on flavor in this measurement, but any differences in the arrival flux of ν_e, ν_μ, ν_τ are taken into account. As the cross section is not flat in each bin, the effect of these four parameters is to convert it into a piecewise function where each piece is independently rescaled. Such an approach introduces discontinuities due to binning but allows for a measurement of the total neutrino-nucleon cross section as a function of energy. It also relaxes constraints based on the overall shape of the CSMS cross section and results in a more model-independent measurement. As the fit proceeds over all four bins simultaneously, bin-to-bin correlations can be examined, though no regularization is applied.

The CSMS cross section is computed for free nucleon targets and does not correct for nuclear shadowing. The shadowing effect modifies nuclear parton densities and is stronger for heavier nuclei. At energies below 100 TeV, antishadowing can increase the cross section by 1%–2%, while above 100 TeV, shadowing can decrease the cross section by 3%–4% [38]. As this is a subdominant effect, we do not include it in this analysis. We do, however, consider the Glashow resonance in which an incident $\bar{\nu}_e$ creates an on-shell W^- by scattering off an electron in the detector.

The effect on the expected arrival flux at the detector due to a modified cross section is calculated with nuSQuIDS, a

TABLE I. Central values and uncertainties on the nuisance parameters included in the fit. Truncated Gaussians are set to zero outside the range. These modify the likelihood used in both the Bayesian and frequentist constructions. Their best-fit values over the likelihood space are also given.

Parameter	Constraint/prior	Range	Shape	Best fit
<i>Astrophysical ν:</i>				
Φ_{astro}	...	$[0, \infty)$	Uniform	6.94
γ_{astro}	2.0 ± 1.0	$(-\infty, \infty)$	Gaussian	3.15
<i>Atmospheric ν:</i>				
Φ_{conv}	1.0 ± 0.4	$[0, \infty)$	Truncated	0.96
Φ_{prompt}	1.0 ± 3.0	$[0, \infty)$	Truncated	0.00
π/K	1.0 ± 0.1	$[0, \infty)$	Truncated	1.00
$2\nu/(\nu + \bar{\nu})_{\text{atmo}}$	1.0 ± 0.1	$[0, 2]$	Truncated	1.00
<i>Cosmic ray:</i>				
$\Delta\gamma_{\text{CR}}$	-0.05 ± 0.05	$(-\infty, \infty)$	Gaussian	-0.05
Φ_μ	1.0 ± 0.5	$[0, \infty)$	Truncated	1.22

neutrino propagation framework that properly takes into account destructive CC interactions, cascading NC interactions, and tau-regeneration effects [39]. A forward-folded fit is then performed, relying on MC to map each neutrino flavor to the experimental PID of tracks, cascades and double cascades [36], in the reconstructed zenith vs reconstructed energy distribution for tracks and cascades and in the reconstructed energy vs cascade length separation distribution for double cascades [28]. The fit uses the Poisson-like likelihood, \mathcal{L}_{eff} , which accounts for statistical uncertainties in the MC and is constructed by comparing the binned MC to data [34]. The ternary PID of tracks, cascades, and double cascades is an additional constraint to the fit, which allows this measurement to incorporate interaction characteristics of all three neutrino flavors [36]. Using MC simulations, we can account for deviations between the true flavor and the PID and also estimate its accuracy. Under best-fit expectations, true ν_e are classified as cascades approximately 57% of the time, true ν_μ as tracks approximately 73% of the time, and true ν_τ as double cascades approximately 65% of the time [28].

Systematic uncertainties are incorporated via the parameters listed in Table I. The parameter Φ_{conv} (Φ_{prompt}) linearly scales the atmospheric neutrino flux normalization for neutrinos produced by π or K (charm meson) decay [40,41]. The parameters γ and Φ_{astro} modify the spectral index and normalization of the astrophysical neutrino flux, respectively. The parameter Φ_μ linearly scales the atmospheric muon flux normalization. The ratio of atmospheric neutrinos produced in pion vs kaon decay is governed by the π/K parameter. The parameter $\nu/\bar{\nu}$ governs the ratio of atmospheric neutrinos to antineutrinos. Finally, the parameter $\Delta\gamma_{\text{CR}}$ modifies the spectral index of the cosmic-ray flux [42]. Detector systematic studies were performed using Asimov data but had a negligible impact on the result. Priors on the nuisance parameters are given in Table I. The

prior on γ_{astro} is driven by the usual Fermi acceleration mechanism, allowing for a large uncertainty that covers those reported in a previous and independent IceCube measurement of the diffuse neutrino flux [43]. Such a large uncertainty minimizes the impact of changing the central value on the measured cross section. None of the x_i parameters shifted by more than 1% in postunblinding checks where $\gamma_{\text{astro}} = 3.0 \pm 1.0$.

Out of all the nuisance parameters, γ_{astro} and Φ_{astro} exhibited the largest correlation with the cross section parameters. They are most strongly correlated with x_0 , the cross section in the lowest-energy bin. This is believed to be related to the fact that lower-energy neutrinos are subject to less Earth absorption so the main effect of varying the low-energy cross section is a near-linear scaling at the detector. This makes x_0 essentially inversely proportional to the astrophysical flux. By allowing the cross section to float, the data seem to prefer the softer index, as given in Table I.

The interaction rate of high-energy neutrinos traveling through the Earth is also dependent on the Earth density. Here, we fix the density to the preliminary reference Earth model [44]. This is a parametric description of the density as a function of radial distance from the center of the Earth, evaluated using several sources of surface and body seismic wave data. Since the density uncertainty is at the few percent level, it is negligible in comparison to the flux uncertainty and is fixed for the purposes of this measurement [45].

Note that the Glashow resonance occurs for an incident $\bar{\nu}_e$ with an energy around 6.3 PeV and is not varied in the fit as it is calculable from first principles, using the known decay width of the W boson. However, unlike high-energy neutrino-nucleon scattering, the expected number of events due to the Glashow resonance is strongly dependent on the ratio of neutrinos and antineutrinos in the incident flux. We therefore performed a test that varied the astrophysical flux from a pure neutrino flux to a pure antineutrino flux. It was found only to have a minimal effect in the highest-energy bin, where the measurement uncertainty is largest. This is due in part to the steeply falling spectrum, which causes the flux at 6.3 PeV to be much smaller than that at lower energies. As the effect on the cross section is minimal, we keep the ratio of the flux of astrophysical neutrinos and antineutrinos fixed to unity.

We report both Bayesian highest posterior density (HPD) credible intervals and frequentist confidence intervals (CI). In the Bayesian construction, the posterior on the four scaling parameters is obtained with a Markov chain Monte Carlo (MCMC) sampler, emcee, marginalizing over nuisance parameters [46]. A uniform prior from 0 to 50 is assumed for all four cross section scaling parameters. Such a prior gives more weight to parameter values greater than 1. To test its effect, the MCMC was also run assuming a log-uniform prior, which gives results consistent with those assuming a uniform prior. The

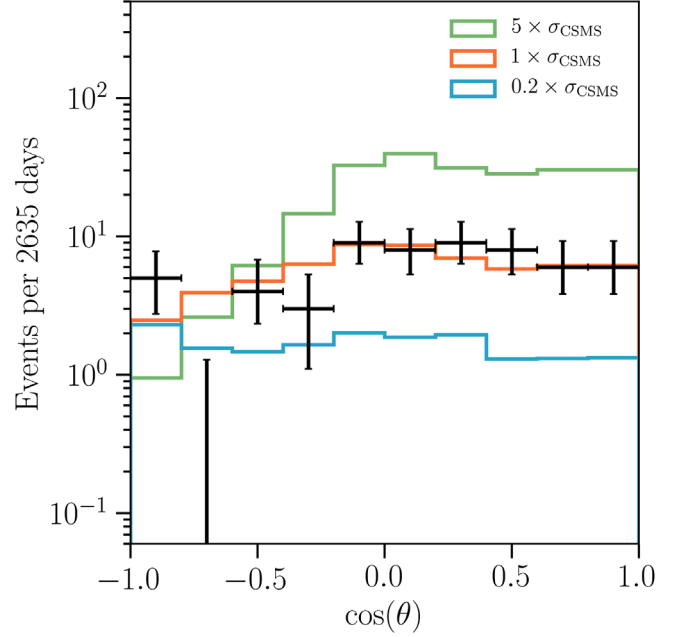


FIG. 3. The zenith distribution of data and the best-fit, single-power-law flux expectation assuming σ_{CSMS} (orange) [2]. Predictions from two alternative cross sections are shown as well, assuming the same flux. In the Southern sky, $\cos \theta > 0$, the Earth absorption is negligible, so the effect of rescaling the cross section is linear. In the Northern sky, $\cos \theta < 0$, the strength of Earth absorption is dependent on the cross section as well as the neutrino energy and zenith angle.

MCMC is sampled with 60 walkers over 5000 total steps, the first 1000 of which are treated as part of the initialization stage and discarded.

The frequentist confidence regions are obtained from a grid scan of the likelihood across four dimensions, profiling over the nuisance parameters and assuming Wilks theorem. For x_0 , x_1 , and x_2 , 15 equal-distant points are used from 0.1 to 5. For x_3 , 29 equal-distant points are used from 0.1 to 9.9. For each \mathbf{x} on the mesh of these points, the likelihood is minimized over all other nuisance parameters. Confidence regions in two or one dimension are then evaluated by profiling across the other cross section parameters followed by application of Wilks theorem. Though the best-fit $\Phi_{\text{prompt}} = 0$, the prompt component is expected to be a small contribution to the overall distribution. Thus, we expect Wilks theorem to hold asymptotically in the high statistics limit.

The zenith-dependent effect of the cross section on the event rate is shown in Fig. 3, assuming the best-fit, single-power-law flux reported in Ref. [28], which is obtained using the CSMS cross section $\sigma = \sigma_{\text{CSMS}}$ [2]. The degeneracy in the measurements of flux and cross section is broken by the different amounts of matter traversed by neutrinos arriving from different directions. To illustrate the effect of a modified cross section, two alternative expectations are shown for $\sigma = 0.2\sigma_{\text{CSMS}}$ and $\sigma = 5\sigma_{\text{CSMS}}$ under

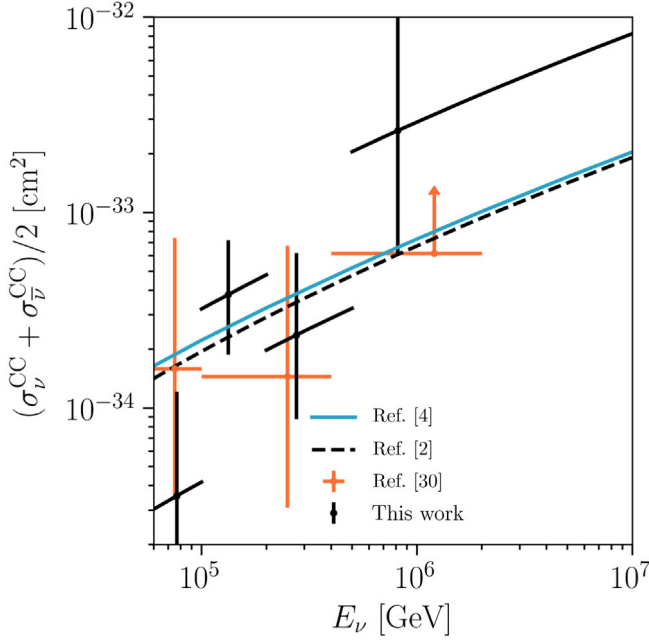


FIG. 4. The charged-current, high-energy neutrino cross section as a function of energy, averaged over ν and $\bar{\nu}$. The Bayesian 68.3% HPD credible interval is shown along with two cross section calculations [2,4]. The credible intervals from a previous analysis [30] are also shown for comparison.

the same best-fit flux assumption. In the Southern sky ($\cos\theta > 0$), the Earth absorption is negligible, and the event rate is simply proportional to the cross section. In the Northern sky ($\cos\theta < 0$), the strength of Earth absorption is dependent on the zenith angle, E_ν , and the cross section. Absorption alters the shape of the event-rate zenith distribution in the Northern sky. For example, with $\sigma = 5\sigma_{\text{CSMS}}$ and near $\cos\theta = -0.5$, the attenuation of the arriving flux counteracts the increased neutrino interaction probability so that the event rate falls back to that expected from the CSMS cross section. Modifications of the neutrino cross section are thus constrained by the nonobservation of energy-dependent distortions in the zenith angle distribution.

IV. RESULTS

The CC cross section, averaged over ν and $\bar{\nu}$, is shown in black in Figs. 4 and 5 for the Bayesian 68.3% HPD and frequentist one sigma intervals assuming Wilks theorem, respectively. As the scale factor is applied across the entire interval within an energy bin on the CSMS calculations, the shape is preserved within each bin. The central point in each energy bin corresponds to the expected, most probable energy in $dN_{\text{MC}}/d\log E$, the distribution of events in the MC along the x axis. This is chosen in lieu of the linear or logarithmic bin center to better represent where most of the statistical power lies in each bin. Since we assume a fixed CC-NC cross section ratio, the NC cross section is the same

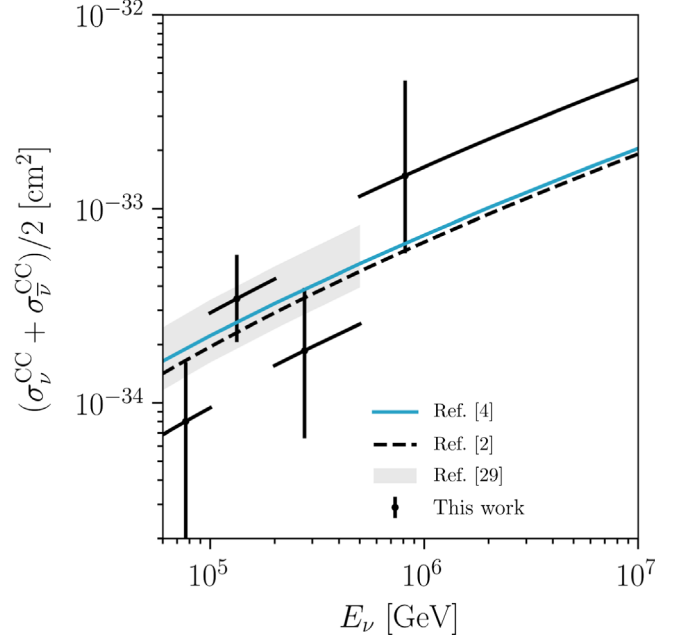


FIG. 5. The charged-current, high-energy neutrino cross section as a function of energy, averaged over ν and $\bar{\nu}$. The Wilks 1-sigma CI is shown along with two cross section calculations [2,4]. The confidence intervals from Ref. [29] are also shown for comparison.

result relative to the CSMS prediction and so is not shown here.

In addition, the measurement based on HESE showers with 6 years of data is shown as orange crosses [30] in

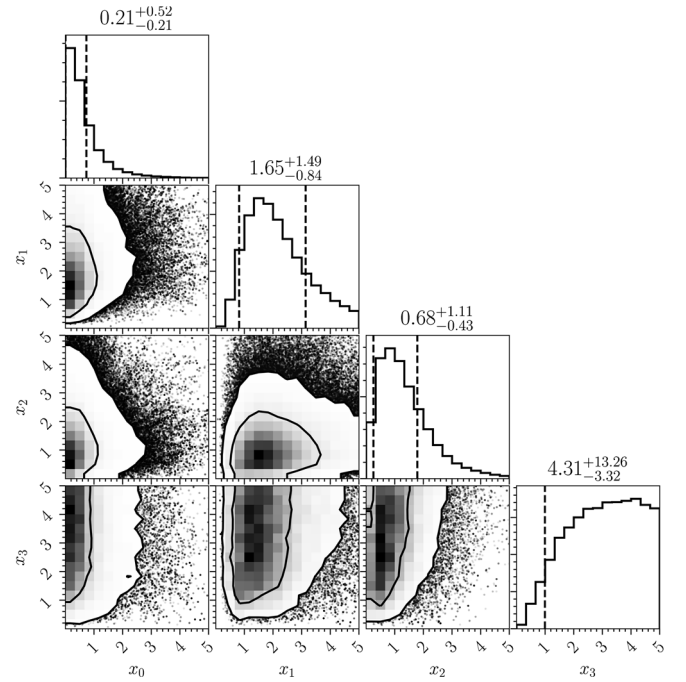


FIG. 6. The full posterior distribution of \mathbf{x} as evaluated with emcee [46]. In the two-dimensional distributions, the 68.3% and 95.4% HPD regions are shown. In the one-dimensional distribution, the 68.3% HPD interval is indicated by the dashed lines.

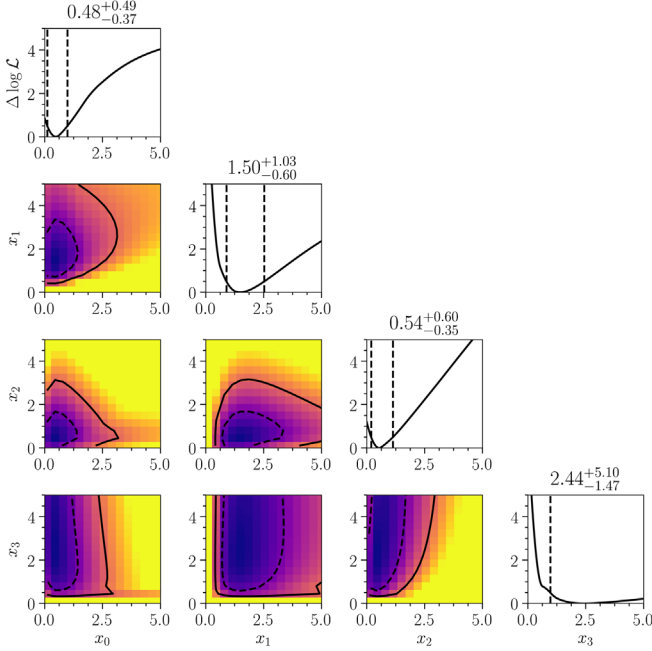


FIG. 7. The profile likelihood of \mathbf{x} as evaluated with the grid scan over \mathbf{x} . In the two-dimensional figures, the Wilks 68.3% and 95.4% confidence regions are shown as dashed and solid lines, respectively. In the one-dimensional plots of $\Delta \log \mathcal{L}$, the 68.3% confidence interval is indicated by the dashed lines.

Fig. 4, and the previously published IceCube measurement, using up-going muon-neutrinos, is shown as the shaded gray region [29] in Fig. 5. Since credible intervals and confidence intervals have different interpretations, we do not plot them on the same figure. Note that both previous measurements extend below 60 TeV and are truncated in this comparison. Predictions from Refs. [2] and [4] are shown as the dashed and solid lines, respectively.

A corner plot of the posterior density, marginalized over all except two or one of the cross section parameters, is shown in Fig. 6. Similarly, two-dimensional profile likelihoods are shown in Fig. 7. Both exhibit little correlation between the various cross section parameters. The largest uncertainty arises for x_3 , which has the widest posterior distribution and flattest profile likelihood.

The Bayesian and frequentist results are consistent with each other, though again we caution that their intervals cannot be interpreted in the same manner. The results are

TABLE II. Measured 68.3% HPD (Bayesian) and CI (frequentist) for the four cross section parameters.

Parameter	Energy range	68.3% HPD	68.3% CI
x_0	60 TeV to 100 TeV	$0.21^{+0.52}_{-0.21}$	$0.48^{+0.49}_{-0.37}$
x_1	100 TeV to 200 TeV	$1.65^{+1.49}_{-0.84}$	$1.50^{+1.03}_{-0.60}$
x_2	200 TeV to 500 TeV	$0.68^{+1.11}_{-0.43}$	$0.54^{+0.60}_{-0.35}$
x_3	500 TeV to 10 TeV	$4.31^{+13.26}_{-3.32}$	$2.44^{+5.10}_{-1.47}$

compatible with the Standard Model and are summarized in Table II.

V. CONCLUSIONS

We have described a measurement of the neutrino DIS cross section using the IceCube detector. Variations in the neutrino cross section from Standard Model predictions modify the expected flux and event rate at our detector, and a sample of high-energy events starting within the fiducial volume of IceCube has been utilized to thus measure the neutrino cross section. Previous TeV–PeV scale neutrino cross sections have been measured by IceCube [29] using a sample of through-going muons and with cascades in the HESE sample [30]. This result, however, is the first measurement of the neutrino DIS cross section to combine information from all three neutrino flavors.

Our results are compatible with Standard Model predictions, though the data seem to prefer smaller values at the lowest-energy bin and higher values at the highest-energy bin. There do not seem to be strong correlations between the cross section bins, though large uncertainties due to a dearth of data statistics make it difficult to draw strong conclusions. With additional data, or with a combined fit across multiple samples, more precise measurements are foreseen in the near future [47].

ACKNOWLEDGMENTS

The IceCube Collaboration acknowledges the significant contributions to this manuscript from Tianlu Yuan. The authors gratefully acknowledge the support from the following agencies and institutions: U.S. National Science Foundation–Office of Polar Programs, U.S. National Science Foundation–Physics Division, Wisconsin Alumni Research Foundation, Center for High Throughput Computing (CHTC) at the University of Wisconsin–Madison, Open Science Grid (OSG), Extreme Science and Engineering Discovery Environment (XSEDE), U.S. Department of Energy–National Energy Research Scientific Computing Center, Particle astrophysics research computing center at the University of Maryland, Institute for Cyber-Enabled Research at Michigan State University, and Astroparticle physics computational facility at Marquette University (USA); Funds for Scientific Research (FRS-FNRS and FWO), FWO Odysseus and Big Science programs, and Belgian Federal Science Policy Office (Belspo) (Belgium); Bundesministerium für Bildung und Forschung (BMBF), Deutsche Forschungsgemeinschaft (DFG), Helmholtz Alliance for Astroparticle Physics (HAP), Initiative and Networking Fund of the Helmholtz Association, Deutsches Elektronen Synchrotron (DESY), and High Performance Computing cluster of the RWTH Aachen (Germany); Swedish Research Council, Swedish Polar Research Secretariat, Swedish National Infrastructure

for Computing (SNIC), and Knut and Alice Wallenberg Foundation (Sweden); Australian Research Council (Australia); Natural Sciences and Engineering Research Council of Canada, Calcul Québec, Compute Ontario, Canada Foundation for Innovation, WestGrid, and Compute Canada (Canada); Villum Fonden, Danish National Research Foundation (DNRF), Carlsberg

Foundation (Denmark); Marsden Fund (New Zealand); Japan Society for Promotion of Science (JSPS) and Institute for Global Prominent Research (IGPR) of Chiba University (Japan); National Research Foundation of Korea (NRF) (Korea); Swiss National Science Foundation (SNSF) (Switzerland); Department of Physics, University of Oxford (United Kingdom).

-
- [1] R. Gandhi, C. Quigg, M. H. Reno, and I. Sarcevic, Ultra-high-energy neutrino interactions, *Astropart. Phys.* **5**, 81 (1996).
 - [2] A. Cooper-Sarkar, P. Mertsch, and S. Sarkar, The high energy neutrino cross-section in the Standard Model and its uncertainty, *J. High Energy Phys.* **08** (2011) 042.
 - [3] A. Connolly, R. S. Thorne, and D. Waters, Calculation of High Energy Neutrino-Nucleon Cross Sections and Uncertainties Using the MSTW Parton Distribution Functions and Implications for Future Experiments, *Phys. Rev. D* **83**, 113009 (2011).
 - [4] C. A. Argüelles, F. Halzen, L. Wille, M. Kroll, and M. H. Reno, High-energy behavior of photon, neutrino, and proton cross sections, *Phys. Rev. D* **92**, 074040 (2015).
 - [5] P. Jain, D. W. McKay, S. Panda, and J. P. Ralston, Extra dimensions and strong neutrino nucleon interactions above 10^{19} -eV: Breaking the GZK barrier, *Phys. Lett. B* **484**, 267 (2000).
 - [6] J. Alvarez-Muniz, J. L. Feng, F. Halzen, T. Han, and D. Hooper, Detecting microscopic black holes with neutrino telescopes, *Phys. Rev. D* **65**, 124015 (2002).
 - [7] I. Romero and O. A. Sampayo, Leptoquarks signals in KM^3 neutrino telescopes, *J. High Energy Phys.* **05** (2009) 111.
 - [8] J. Ellis, K. Sakurai, and M. Spannowsky, Search for sphalerons: IceCube vs. LHC, *J. High Energy Phys.* **05** (2016) 085.
 - [9] A. R. Bell, The acceleration of cosmic rays in shock fronts. I, *Mon. Not. R. Astron. Soc.* **182**, 147 (1978).
 - [10] R. D. Blandford and J. P. Ostriker, Particle acceleration by astrophysical shocks, *Astrophys. J. Lett.* **221**, L29 (1978).
 - [11] F. Halzen and D. Saltzberg, Tau-Neutrino Appearance with a 1000 Megaparsec Baseline, *Phys. Rev. Lett.* **81**, 4305 (1998).
 - [12] J. A. Formaggio and G. P. Zeller, From eV to EeV: Neutrino cross sections across energy scales, *Rev. Mod. Phys.* **84**, 1307 (2012).
 - [13] A. C. Vincent, C. A. Argüelles, and A. Kheirandish, High-energy neutrino attenuation in the Earth and its associated uncertainties, *J. Cosmol. Astropart. Phys.* **11** (2017) 012.
 - [14] S. L. Glashow, Resonant scattering of antineutrinos, *Phys. Rev.* **118**, 316 (1960).
 - [15] D. Seckel, Neutrino Photon Reactions in Astrophysics and Cosmology, *Phys. Rev. Lett.* **80**, 900 (1998).
 - [16] I. Alikhanov, The Glashow resonance in neutrino-photon scattering, *Phys. Lett. B* **741**, 295 (2015).
 - [17] I. Alikhanov, Hidden Glashow resonance in neutrino-nucleus collisions, *Phys. Lett. B* **756**, 247 (2016).
 - [18] B. Zhou and J. F. Beacom, Neutrino-nucleus cross sections for W-boson and trident production, *Phys. Rev. D* **101**, 036011 (2020).
 - [19] M. G. Aartsen *et al.* (IceCube-Gen2 Collaboration), IceCube-Gen2: The window to the extreme universe, *J. Phys. G: Nucl. Part. Phys.* **48**, 060501 (2021).
 - [20] B. Zhou and J. F. Beacom, W-boson and trident production in TeV–PeV neutrino observatories, *Phys. Rev. D* **101**, 036010 (2020).
 - [21] M. G. Aartsen *et al.* (IceCube Collaboration), First Observation of PeV-Energy Neutrinos with IceCube, *Phys. Rev. Lett.* **111**, 021103 (2013).
 - [22] M. G. Aartsen *et al.* (IceCube Collaboration), Evidence for High-Energy Extraterrestrial Neutrinos at the IceCube Detector, *Science* **342**, 1242856 (2013).
 - [23] M. G. Aartsen *et al.* (IceCube Collaboration), Atmospheric and astrophysical neutrinos above 1 TeV interacting in IceCube, *Phys. Rev. D* **91**, 022001 (2015).
 - [24] M. G. Aartsen *et al.* (IceCube Collaboration), Observation of High-Energy Astrophysical Neutrinos in Three Years of IceCube Data, *Phys. Rev. Lett.* **113**, 101101 (2014).
 - [25] R. Abbasi *et al.* (IceCube Collaboration), The IceCube data acquisition system: Signal capture, digitization, and time-stamping, *Nucl. Instrum. Methods Phys. Res., Sect. A* **601**, 294 (2009).
 - [26] R. Abbasi *et al.* (IceCube Collaboration), Calibration and characterization of the icecube photomultiplier tube, *Nucl. Instrum. Methods Phys. Res., Sect. A* **618**, 139 (2010).
 - [27] M. G. Aartsen *et al.* (IceCube Collaboration), The IceCube neutrino observatory: Instrumentation and online systems, *J. Instrum.* **12**, P03012 (2017).
 - [28] R. Abbasi *et al.* (IceCube Collaboration), following paper, The IceCube high-energy starting event sample: Description and flux characterization with 7.5 years of data, *Phys. Rev. D* **103**, 022002 (2021).
 - [29] M. G. Aartsen *et al.* (IceCube Collaboration), Measurement of the multi-TeV neutrino cross section with IceCube using Earth absorption, *Nature (London)* **551**, 596 (2017).
 - [30] M. Bustamante and A. Connolly, Extracting the Energy-Dependent Neutrino-Nucleon Cross Section Above 10 TeV Using IceCube Showers, *Phys. Rev. Lett.* **122**, 041101 (2019).

- [31] D. Chirkin (IceCube Collaboration), Evidence of optical anisotropy of the South Pole ice, in *33rd International Cosmic Ray Conference* (Rio de Janeiro, Brazil, 2013), pp. 415–608.
- [32] D. Chirkin and M. Rongen (IceCube Collaboration), Light diffusion in birefringent polycrystals and the IceCube ice anisotropy, *Proc. Sci., ICRC2019* (**2020**) 854 [[arXiv: 1908.07608](#)].
- [33] C. A. Argüelles, S. Palomares-Ruiz, A. Schneider, L. Wille, and T. Yuan, Unified atmospheric neutrino passing fractions for large-scale neutrino telescopes, *J. Cosmol. Astropart. Phys.* **07** (2018) 047.
- [34] C. A. Argüelles, A. Schneider, and Tianlu Yuan, A binned likelihood for stochastic models, *J. High Energy Phys.* **06** (2019) 030.
- [35] M. G. Aartsen *et al.* (IceCube Collaboration), Measurement of Atmospheric Neutrino Oscillations at 6–56 GeV with IceCube DeepCore, *Phys. Rev. Lett.* **120**, 071801 (2018).
- [36] M. Usner, Search for astrophysical tau-neutrinos in six years of high-energy starting events in the icecube detector, Ph.D. thesis, Humboldt University, Berlin, 2018.
- [37] J. S. Gainer, J. Lykken, K. T. Matchev, S. Mrenna, and M. Park, Exploring theory space with Monte Carlo reweighting, *J. High Energy Phys.* **10** (2014) 078.
- [38] S. R. Klein, S. A. Robertson, and R. Vogt, Nuclear effects in high-energy neutrino interactions, *Phys. Rev. C* **102**, 015808 (2020).
- [39] C. A. Argüelles Delgado, J. Salvado, and C. N. Weaver, A simple quantum integro-differential solver (SQuIDS), *Comput. Phys. Commun.* **196**, 569 (2015).
- [40] M. Honda, T. Kajita, K. Kasahara, S. Midorikawa, and T. Sanuki, Calculation of atmospheric neutrino flux using the interaction model calibrated with atmospheric muon data, *Phys. Rev. D* **75**, 043006 (2007).
- [41] A. Bhattacharya, R. Enberg, M. H. Reno, I. Sarcevic, and A. Stasto, Perturbative charm production and the prompt atmospheric neutrino flux in light of RHIC and LHC, *J. High Energy Phys.* **06** (2015) 110.
- [42] T. K. Gaisser, T. Stanev, and S. Tilav, Cosmic ray energy spectrum from measurements of air showers, *Front. Phys. (Beijing)* **8**, 748 (2013).
- [43] M. G. Aartsen *et al.* (IceCube Collaboration), Observation and Characterization of a Cosmic Muon Neutrino Flux from the Northern Hemisphere using six years of IceCube data, *Astrophys. J.* **833**, 3 (2016).
- [44] A. M. Dziewonski and D. L. Anderson, Preliminary reference earth model, *Phys. Earth Planet. Interiors* **25**, 297 (1981).
- [45] B. L. N. Kennett, On the density distribution within the earth, *Geophys. J. Int.* **132**, 374 (1998).
- [46] D. Foreman-Mackey, D. W. Hogg, D. Lang, and J. Goodman, emcee: The MCMC Hammer, *Publ. Astron. Soc. Pac.* **125**, 306 (2013).
- [47] S. Robertson (IceCube Collaboration), Measurement of the multi-TeV neutrino cross section with IceCube using Earth absorption, *Proc. Sci., ICRC2019* (**2020**) 990 [[arXiv: 1908.06123](#)].